ACS OMEGA

http://pubs.acs.org/journal/acsodf
Article

Hydrothermal Synthesis of Co-MoS_2 as a Bifunctional Catalyst for Overall Water Splitting

Wei Liu,* Linping Fu, Shenshen Yang, Yaozong Lu, Ming Li, Longhua Zhang, and Jiaqi Tang

Cite This: *ACS Omega* 2025, 10, 15129−15142

Read Online

ACCESS | Metrics & More | Article Recommendations | Supporting Information

ABSTRACT: The sluggish kinetics of the oxygen evolution reaction is the main obstacle to the development of water splitting. MoS_2 exhibits excellent activity in hydrogen evolution reaction (HER). However, the catalytic activity is insufficient for commercial bifunctional catalysts due to the inadequate oxygen evolution reaction (OER) catalytic activity. To address the deficiency of the OER active site of MoS_2 and develop a more effective bifunctional catalyst, a one-step hydrothermal process was employed to synthesize a nonprecious Co−MoS_2 catalyst, utilizing sodium molybdate as the molybdenum source, thiourea as the sulfur source, and cobalt nitrate as the cobalt source, respectively. The electrocatalytic activity of the sample was tested in an electrolyte solution of 0.1 M KOH and 1 M KOH. The experimental result indicated that the catalytic activity of the Co−MoS_2 catalyst for HER and OER was remarkably enhanced compared to the pristine MoS_2. The overpotential of OER and HER was reduced by approximately 200 mV and 130 mV in a 0.1 M KOH solution, respectively. Additionally, in the 1 M KOH electrolyte, the overpotentials of OER and HER were about 312 mV and 297 mV, respectively. Co−MoS_2 with the $Co(NO_3)_2$ doping of 0.6 g (0.206 mol %) also exhibited excellent stability in 0.1 M KOH and 1 M KOH electrolytes. When the Co−MoS_2 ($Co(NO_3)_2$—0.6 g, 0.343 mol %) electrode was used as both anode and cathode for overall water splitting in the 1 M KOH electrolyte, the current density of 10 mA cm^{-2} could be achieved with only 1.86 V and with a good stability. This work provides an alternative for bifunctional catalysts in overall water splitting.

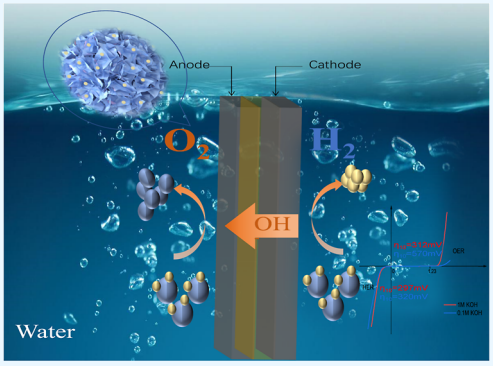

1. INTRODUCTION

Energy and the environment are two key issues for the sustainable development of human society.[1] At present, traditional fossil fuels are still the main sources of energy and will eventually be exhausted by continuous consumption. In addition, the greenhouse gases released during the combustion of fossil fuels have caused serious environmental pollution.[2−8] Therefore, finding new energy sources to replace fossil fuels is highly desirable.[9,10] In recent decades, various renewable energy sources have been explored.[11−13] Among these clean energy sources, hydrogen energy has attracted much attention due to its nontoxic emission and high energy density.

Water electrolysis technology is an important method for the production of high-purity hydrogen and a crucial component of energy systems.[14] The water splitting involves two reaction processes, hydrogen evolution reaction (HER) and oxygen evolution reaction (OER). HER is the reaction of two electrons while OER requires the transfer of four electrons to proceed.[15,16] So OER has to overcome a higher kinetic barrier in water splitting.[17] A higher overpotential means that in industrial operation, additional electrical energy is usually required to overcome the energy barrier, resulting in energy consumption. Therefore, catalysts are needed to improve the reaction rate. To date, the most commonly used electrocatalyst is the precious metal catalyst with scarcity and high cost, limiting their widespread application in the industry.[18] Therefore, most attention is needed to focus on monofunctional catalysts and the majority of the electrocatalysts studied are only suitable for OER or HER under specific alkaline or acidic solutions. The bifunctional catalyst exhibits the dual catalytic ability for both HER and OER in the electrolyzed water process. This unique characteristic provides significant advantages to the electrode in improving the efficiency of water splitting. Therefore, the development of a non-noble metal bifunctional catalyst with excellent electrocatalytic performance has become an urgent issue of overall water splitting for hydrogen production.

Over the decades, researchers have made significant progress in low-cost electrocatalysts, including oxides,[19,20] sulfides,[21,22] and phosphides.[23,24] Among these materials, molybdenum sulfides (MoS_2) and cobalt sulfides(CoS_2) have attracted lots

Received: November 26, 2024
Revised: March 26, 2025
Accepted: April 3, 2025
Published: April 10, 2025

https://doi.org/10.1021/acsomega.4c10747
ACS Omega 2025, 10, 15129−15142

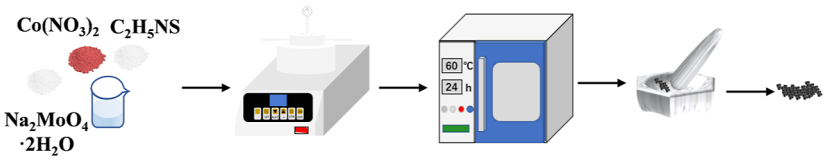

Figure 1. Schematic showing the synthesis of Co−MoS_2.

of attention due to their lower cost and excellent electrocatalytic activity.[25] These properties make them have great potential in water splitting. The two-dimensional MoS_2 is an excellent HER catalyst, due to the similarity of the H* to Pt.[26] However, MoS_2 is a kind of semiconductor with poor electrical conductivity at room temperature. The number of active sites on the basal plane is restricted due to S atoms, which are limited by unsaturated bonds and dangling bonds. In addition, the reaction energy barrier of the OER is higher, resulting in a slower reaction rate in water splitting. Nowadays, the approaches for enhancing the catalytic activity of MoS_2 can be classified into the following categories: (1) exposure of additional active sites,[27,28] (2) composition with a conductive matrix to enhance conductivity,[29,30] (3) improvement of the catalytic activity of the peripheral active sites.[31,32] CoS_2 is an effective electrocatalyst for OER in alkaline solutions. In the OER process, the excellent electrochemical performance of CoS_2 may be attributed to its sulfur-rich nature, the presence of bridged S−S, and more active CoS_6 octahedral coordination. All Co^{2+} in CoS_2 are bonding with S^{2-} in the form of CoS_6 octahedra. Wang[33] et al. found that octahedrally coordinated Co^{n+}(n = 2,3) sites are more active than tetrahedrally coordinated Co^{2+} sites. In addition, with the increase of S atom ratio in cobalt sulfides, the valence state of S will change from S^{2-} to bridged or terminal S_2^{2-} ions,[34] which will further improve the electrochemical activity and catalytic efficiency of cobalt sulfides. On the other hand, the introduction of the Co element can not only regulate the morphology and structure of the MoS_2 crystal lattice but also improve the conductivity.[35] As mentioned above, the effective combination of molybdenum disulfide and cobalt sulfide has the potential to be a valuable substitute in electrocatalysts. Ganesan[36] et al. prepared CoS_2−MoS_2 multishelled hollow spheres as an efficient bifunctional catalyst due to the synergistic effect between CoS_2 and MoS_2.

It is a challenge to achieve equilibrium between the adsorption capacity of OH^- and H* at the same active site. Therefore, the most common strategy for effectively controlling adsorption capacities is to construct dual active sites.[37,38] The incorporation of one catalyst for HER with another catalyst for OER is an efficient approach to designing bifunctional catalytic materials. The synergistic effect between the components enhances the catalytic activity for water splitting. The CoS_2@MoS_2 synthesized by Wang[39] et al. exhibited the overpotential reduced by 54 and 46 mV under acidic and alkaline conditions. Chen[40] et al. synthesized a CoS_2−MoS_2 heterostructure catalyst with MoS_2 nanosheets vertically anchored on CoS_2 microflakes via interfacial engineering, which not only increased the number of exposed active sites and structural defects but also provided a hierarchically porous structure. Relevant pieces of literature show that the hybrid catalyst contained a more pronounced high density of terminal sulfur edge than the bulk MoS_2.[41]

The abundant active sites are attributed to the superior performance of Co−MoS_2. However, further improving the density of active sites remains a challenge. The number of active sites is increased frequently through the strategy of interfacial engineering and morphology regulation. Meanwhile, the introduced concentration and distribution of the Co element also should be optimized to develop high-activity catalysts.

In this work, by an enhanced hydrothermal method,[42,43] the samples of Co−MoS_2 with varying morphologies and particle sizes were synthesized. The introduction of the Co element results in the formation of additional defects and active centers. As a result, it exhibited excellent catalysis and stability under 100 h of OER and HER processing, highly beneficial for water splitting.

2. EXPERIMENTAL SECTION

2.1. Synthesis of Co−MoS_2. Sodium molybdate ($Na_2MoO_4.2H_2O$, Tianjin Hengxin Chemical Co., Ltd.), thiourea (H_2NCSNH_2, Tianjin Hengxin Chemical Co., Ltd.), and an appropriate quantity of cobalt nitrate (Co-$(NO_3)_2.6H_2O$, Shanghai McLean Biochemical Technology Co., Ltd.) were dissolved in 80 mL of deionized water and stirred until a uniform solution with purple-red transparency was formed. Subsequently, the solution was transferred to a 200 mL autoclave with micromagnetic stirring, and the reaction temperature was set for 8 h. Following the completion of the reaction, the solution was cooled to room temperature and then centrifuged by a centrifuge (TG-16, Sichuan Shuke Instrument Co., Ltd.), alternating with deionized water and anhydrous ethanol for 4 times. Finally, the residue was dried at 60 °C in a vacuum dryer oven (DHG-9101, Jiangsu Jinyi Instrument Technology Co., Ltd.) for 12 h. The preparation process is illustrated in Figure 1.

2.2. Characterization of the Co−MoS_2 Composite. The crystal structure of the samples was determined using X-ray diffraction (XRD, D8-Advanced, Bruker, Karlsruhe, Germany), field emission scanning electron microscopy (FESEM, JSM-IT800, Nippon Electronics, Tokyo, Japan), and high-resolution transmission electron microscopy (HRTEM, JEM-F200, JEOL, Tokyo, Japan). The composition and content of the specimens were determined using an energy-dispersive spectrometer (EDS, Falcon, EDAX, Pleasanton, CA, USA). The BET tests were carried out by the surface area and pore size distribution analyzer (BELSORP-max II, Microtrac BEL, Osaka, Japan). Additionally, an X-ray photoelectron spectrometer (XPS, ESCALAB 250Xi K-Alpha +, Thermo Fischer Scientific, Waltham, MA, USA) with Al $K\alpha$ X-ray source was used to analyze both the elemental composition and valence states of the specimens.

2.3. Electrochemical Measurements. For preparation of the catalyst ink, a solution of 3 mg of the sample and 1 mg of carbon black (C, Shanghai McLean Biochemical Technology Co., Ltd.) was prepared by dispersing the substances in 980 μL of a mixed solution composed of deionized water and isopropanol. Following ultrasonic homogenization, 20 μL of 5 wt % Nafion (5 wt %, DuPont, USA) solution was added, resulting in the formation of a homogeneous catalyst solution

https://doi.org/10.1021/acsomega.4c10747
ACS Omega 2025, 10, 15129−15142

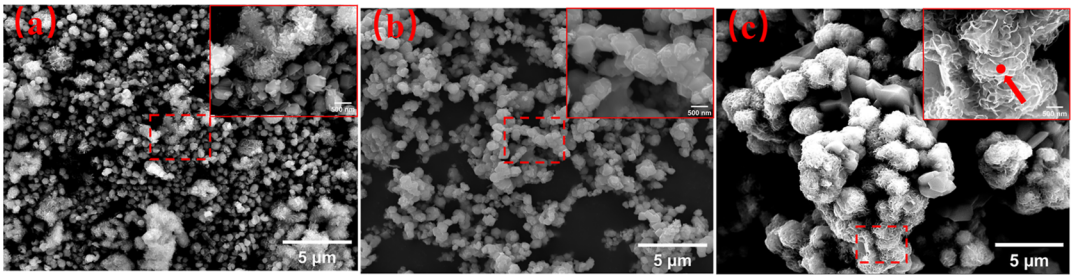

Figure 2. FESEM images of Co−MoS_2 at different reaction temperatures(a-180 °C; b-200 °C; c-220 °C).

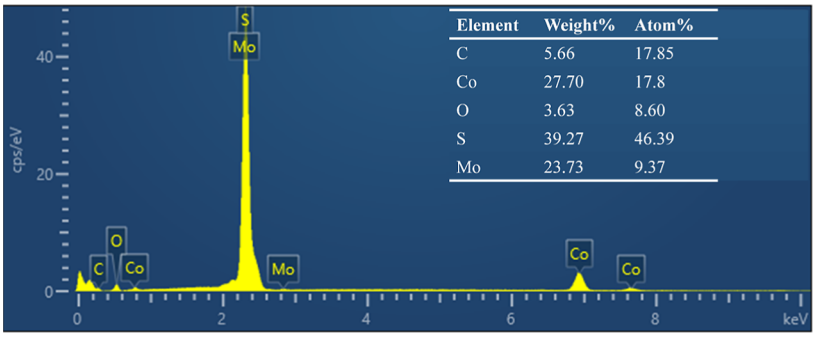

Figure 3. EDS images of Co−MoS_2(220 °C).

through the application of ultrasonication. Twenty μL of the above catalyst solution was dropped on the glassy carbon electrode(S = 0.196 cm^2) and dried in a natural environment.

All electrochemical measurements are conducted using a three-electrode system in an electrochemical workstation, the CHI 660E(Shanghai Chenhua Instrument Co., Ltd.). The glassy carbon electrode (S = 0.196 cm^2) of the drop-coated sample served as the working electrode, a Hg/HgO electrode filled with 1 M KOH was used as the reference electrode, and a Pt sheet with a specification of 10*10*0.2 mm was used as the counter electrode. The electrolyte was composed of 0.1 M KOH. The linear sweep voltammetry (LSV)curves of OER and HER were tested at a scan rate of 5 mV s^{-1}. The measured potential range of the linear sweep voltammetry for HER was −1.6∼-0.8 V(vs Hg/HgO), while the range for OER was 0 ∼ 1 V(vs Hg/HgO). The current was geometrically normalized to the current density, and the measured potential (vs Hg/HgO) was converted into a reversible hydrogen electrode (vs RHE) using the Nernst equation

$$E_{\text{vs.RHE}} = E_{\text{vs.Hg/HgO}} + 0.0592\text{pH} + 0.0977\text{V} \quad (1)$$

All linear sweep voltammograms (LSVs) have been amended by iR compensation. The electrochemical surface area (ECSA) of the catalyst is correlated with the double-layer capacitance (C_{dl}), and CV tests were conducted at varying scan rates (20, 40, 60, 80, and 100 mV s^{-1}). The C_{dl} is related to the scan rate, and the slope of this relationship is indicative of the value of C_{dl}. The frequency range of electrochemical impedance spectroscopy (EIS) is 10^{-1}∼10^6 Hz. The test voltage is defined as the voltage value situated in proximity to the inflection point of the LSV curve, with an amplitude of 5 mV s^{-1}. The stability of OER and HER is characterized by the amperometric curve (i-t), with an overpotential for 100 h.

3. RESULTS AND DISCUSSION

3.1. Crystal Structure, Morphology, and Composition. Figure 2 displays the FESEM images of Co−MoS_2 synthesized with 1g of Na_2MoO_4, 1.8 g of CH_4N_2S, and 0.6 g (0.206 mol %) of $Co(NO_3)_2$ at different temperatures for 8 h. The reaction temperature has a significant influence on the chemical reaction and grain growth rate of crystalline materials. As illustrated in Figure 2a, the sample prepared at 180 °C exhibits two kinds of distinct morphologies. The polyhedron has an approximate particle size of 500 nm, while the flower-like structure is formed by the stacking of sheets with uniform thickness. Upon increasing the temperature to 200 °C, the morphology is exhibited as shown in Figure 2b. The sample exhibits a polyhedron morphology with small sheets of varying particle sizes. Although showing uniform distribution, the particle size of the sample increases compared with that in lower temperatures, accompanied by an increase in the particle agglomeration. As the temperature further rises to 220 °C, the particle microphotograph transformed from polyhedron to nanoflower spheres, stacked by nanosheets, with an approximate diameter of 1 μm. The FESEM images demonstrate that when the synthesis temperature is insufficient (e.g., 180 °C), molecules receive inadequate energy, impeding their ability to attain the energy threshold necessary for the formation of a crystal nucleus. At lower temperatures, the nucleation driving force is weak, which hinders the acceleration of the reaction and diffusion rates. It is difficult to effectively promote the formation of crystal nuclei and the growth of crystals, resulting in a slow and incomplete crystallization process, resulting in two structures of block and fragment. With the rise of temperature (e.g., 200 °C), the movement ability of the reactants is enhanced, which is conducive to more uniform mixing and reaction. However, at this stage, the formation of MoS_2 is limited to the process of formation of CoS_2, resulting in the presentation of flakes. This is confirmed by XRD patterns (Figure 8), in which all diffraction peaks are indexed

https://doi.org/10.1021/acsomega.4c10747
ACS Omega 2025, 10, 15129−15142

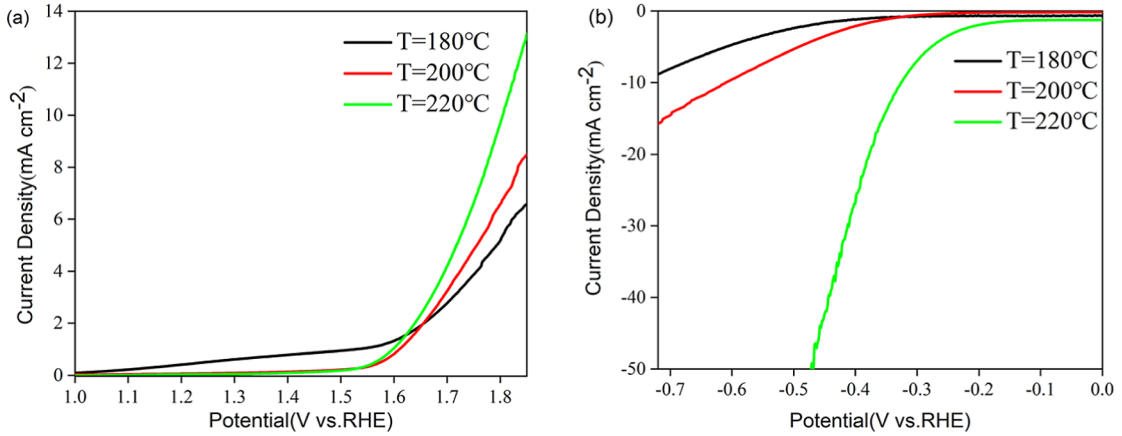

Figure 4. LSV curves of Co−MoS_2 synthesized at different temperatures (a)OER, (b)HER.

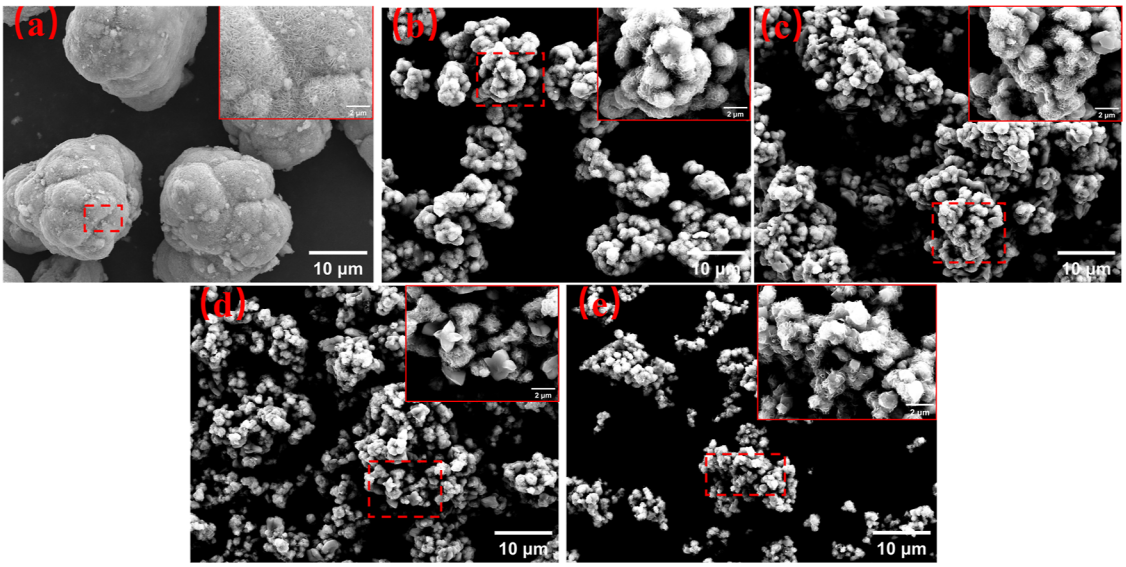

Figure 5. FESEM images of MoS_2 prepared with the different $Co(NO_3)_2$ amounts (a) 0 g (0.000 mol %), (b) 0.4 g (0.137 mol %), (c) 0.6 g (0.206 mol %), (d)0.8 g (0.274 mol %), (e) 1.0 g (0.343 mol %).

to CoS_2 below 200 °C. When the temperature is further increased (e.g., 220 °C), additional nucleation energy is provided for the reactants, resulting in the formation of MoS_2 with CoS_2 as the crystal nucleus. This process generates particles with a nanoflower structure, which is a typical morphology of MoS_2 particles. The EDS analysis of the red point in Figure 2c is presented in Figure 3. The elements of the sample are mainly C, Co, O, S, and Mo, indicating that the Co element has been successfully doped in the MoS_2. As depicted in Figure S3, the elemental mapping images indicate that Mo, S, and Co distribute uniformly in the specimen. In addition, as coated by MoS_2, the signal intensity of Co is relatively low.

The electrocatalytic properties of the samples prepared at 180 °C, 200 °C, and 220 °C were tested using a typical three-electrode apparatus. The LSV curves for OER and HER are shown in Figure 4. It can be found that the Co−MoS_2 specimen prepared at 220 °C shows the best OER electrocatalytic performance, with the lowest overpotential of 570 mV at a current density of 10 mA cm^{-2} (Figure 4a). As the main factors accounting for the OER performance, the crystallinity and content of CoS_2 have remarkable effects on the OER performance due to its distinct characteristics. While the crystallinity of CoS_2 is enhanced at higher temperatures, the overpotential of OER decreases with elevated hydrothermal temperature. As per HER, it shows the same tendency as the OER, as illustrated in Figure 4b. At a current density of −10 mA cm^{-2}, the overpotential is 320 mV, considerably lower than the overpotential of the samples prepared at 200 and 180 °C. As mentioned above, the synthesis temperature is critical for the OER performance. However, due to limitations of the micromagnetic stirring autoclave temperature scale, further exploration at higher temperatures cannot proceed. In summary, the optimal reaction temperature for the synthesis of Co−MoS_2 in this study is 220 °C.

The influence of different $Co(NO_3)_2$ amounts on the microstructure of Co−MoS_2 is also investigated. Figure 5 shows the morphology of the Co−MoS_2 samples, varying addition of $Co(NO_3)_2$ with 0g (0.000 mol %), 0.4 g (0.137 mol %), 0.6 g (0.206 mol %), 0.8 g (0.274 mol %), and 1.0 g (0.343 mol %), respectively. As observed in the FESEM images, the addition of $Co(NO_3)_2$ results in grain refinement and a more uniform distribution of the particle size. The crystal nuclei formation of CoS_2 is more preferentially formed than that of MoS_2, so the small nuclei of CoS_2 emerge in the initial stage of the reaction; consequently, MoS_2 grows on the surface of CoS_2 afterward. The effect of CoS_2 on the crystal growth

https://doi.org/10.1021/acsomega.4c10747
ACS Omega 2025, 10, 15129−15142

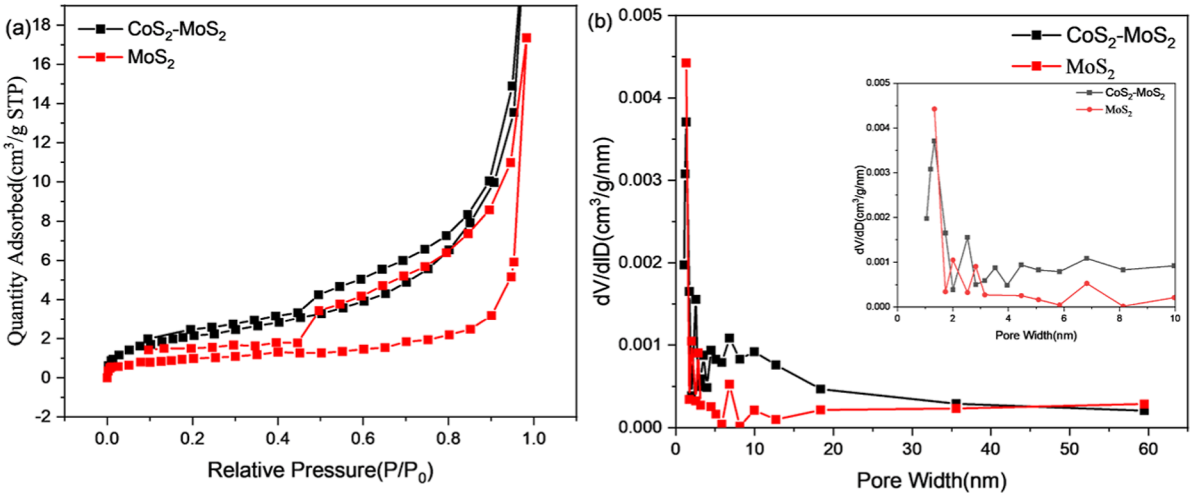

Figure 6. (a)N_2 adsorption−desorption isotherms, (b) pore size distribution of MoS_2 and Co−MoS_2 ($Co(NO_3)_2$—0.6 g, 0.206 mol %).

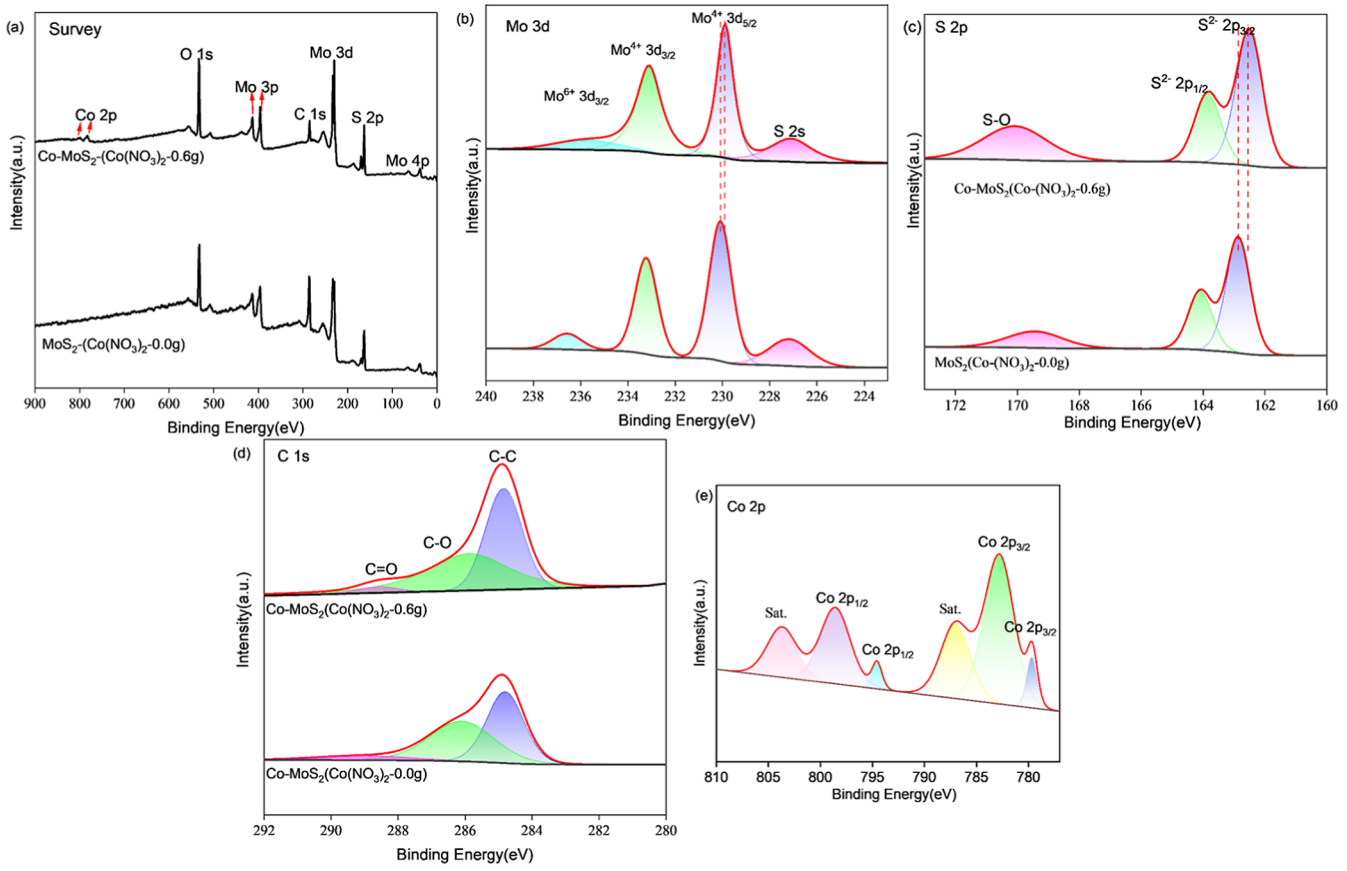

Figure 7. (a) XPS survey spectra of pristine MoS_2 Co−MoS_2($Co(NO_3)_2$—0.6 g, 0.206 mol %) and the refined XPS spectra of (b)Mo 3d, (c)S 2p, (d)C 1s, and (e)Co 2p.

kinetics of MoS_2[44] influences the speed and direction of the latter crystal growth. As a benefit of the small grain size and uniform distribution of CoS_2 nuclei, abundant nuclei are provided for MoS_2 nanosheets to attach and grow, resulting in a smaller grain size. The refined particles increase the specific surface area and enhance the catalytic activity of the material. In addition, doping the Co element also results in a morphology modification of MoS_2. The increasing doping amount of $Co(NO_3)_2$ leading to more sulfur consumption results in less production of MoS_2, which coats the surface of CoS_2 insufficiently. The morphology of MoS_2 changes from the original microflower structure comprising densely stacked nanosheets to the loose stacked structure. When the 1.0 g (0.343 mol %) of $Co(NO_3)_2$ is doped (Figure 5e), the amount of MoS_2 nanosheet is significantly decreased, covering part of the polyhedron.

The N_2 adsorption of pure MoS_2 and Co−MoS_2 ($Co(NO_3)_2$—0.6 g, 0.206 mol %) at 77K was analyzed. The pore volume and pore composition of the material were analyzed. As shown in the figure, the N_2 adsorption−desorption curves

https://doi.org/10.1021/acsomega.4c10747
ACS Omega 2025, 10, 15129−15142

of the samples are typical type IV adsorption isotherms. From the pore size distribution map (Figure 6), it can be seen that the pore size distribution of the synthesized Co−MoS_2(Co-$(NO_3)_2$—0.6 g,0.206 mol %) is relatively uniform, concentrated at 2 and 6 nm, indicating that it is a mesoporous material. The BET specific surface area of the material is 8.1061 $m^2\ g^{-1}$. Compared with the BET specific surface area of pristine MoS_2 (3.6374 $m^2\ g^{-1}$), the introduction of cobalt element increases the specific surface area. The increase of specific surface area after the formation of the composite material may be due to the synergistic effect between cobalt disulfide and molybdenum disulfide. The formation of cobalt disulfide may enhance the dispersion of molybdenum disulfide crystals, so that it exposes more active sites, thereby increasing the specific surface area.

The chemical composition and surface element valence of Co−MoS_2 were further analyzed by X-ray photoelectron spectroscopy (XPS). A typical XPS survey spectrum of the Co−MoS_2 ($Co(NO_3)_2$—0.6 g, 0.206 mol %) and pristine MoS_2, as illustrated in Figure 7a, reveals the presence of the elements C, O, S, Co, and Mo. The Mo 3d spectrum is illustrated in Figure 7b. The peaks at 229.92 and 233.08 eV correspond to Mo $3d_{5/2}$ and Mo $3d_{3/2}$ of Mo^{4+},[45,46] respectively. However, the peak at 235.75 eV is attributed to Mo^{6+} $3d_{3/2}$, indicating part of Mo^{4+} is oxidized to Mo^{6+} ions.[45] However, a large peak area indicates that Mo^{4+} accounts for the majority of the Mo element. Moreover, there is a S 2s peak at the low binding energy of 227.15 eV, which can be attributed to the Mo−S bond and serves as evidence for the presence of MoS_2[37]. Moreover, the peak position of Mo^{4+} $3d_{5/2}$ demonstrates a propensity to shift toward lower binding energy, thereby indicating that the introduction of Co element changes the electronic structure of Mo. This is due to the strong coupling between different components at the interface that leads to the transfer of electrons from MoS_2 to CoS_2[17]. The redistribution of charge resulting from strong electron interaction has been demonstrated to be advantageous in the regulation of the chemical environment of metal sites. This change was usually conducive to the adsorption and desorption of intermediates on the surface of catalyst.[4] The S 2p spectrum (Figure 7d) displays peaks position at 162.22 and 163.84 eV, respectively, attributed to MoS_2[26]. Additionally, the S−O peak at 168.42 eV is ascribed to the surface oxidation of the sample.[45] In comparison with pristine MoS_2, the peaks position of $S^{2-}2p_{2/3}$ in Co−MoS_2($Co(NO_3)_2$—0.6 g, 0.206 mol %) marginally shift toward lower binding energy, indicating a higher prevalence of S vacancies in Co−MoS_2($Co(NO_3)_2$—0.6 g, 0.206 mol %) compared to pristine MoS_2. The C 1s spectrum is illustrated in Figure 7d. The binding energies at 284.83 and 285.93 eV are assigned to the C−C bond and C−O bond, respectively, and 288.61 eV is assigned to the C = O bond.[47] The refined XPS spectrum of Co 2p is illustrated in Figure 7e. The obtained spectrum reveals the presence of satellite peaks at 785.55 and 803.64 eV[48]. The characteristic peaks at 794.18 and 778.91 eV correspond to Co $2p_{3/2}$ and Co $2p_{1/2}$, which are indexed to the Co^{4+} of CoS_2, respectively.[48−50] The peaks at 782.29 and 798.48 eV are indicative of Co^{2+} with oxidation states at the Co $2p_{3/2}$ and Co $2p_{1/2}$ levels, respectively.[10,51]

3.2. Structure and Synthesis Mechanism. The crystal structures of Co−MoS_2 samples prepared at different temperatures were determined by XRD (Figure 8). The diffraction peak of samples synthesized at 180 °C exhibits low intensity,

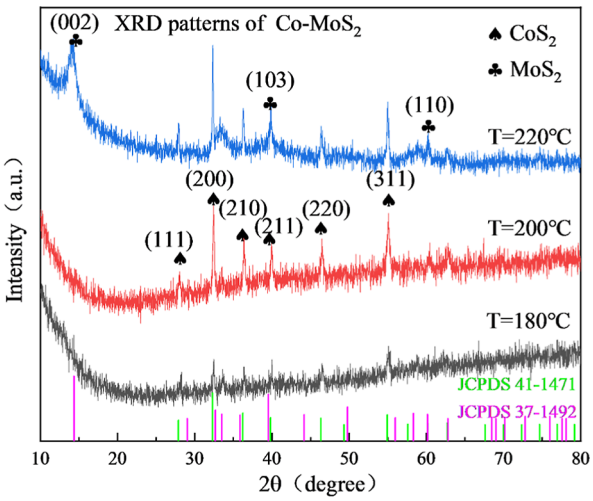

Figure 8. XRD patterns of Co−MoS_2 synthesized at different temperatures.

indicating poor crystallinity of the samples. The diffraction peaks at 2θ = 27.88°, 32.30°, 36.24°, 39.83°, 46.32°, and 54.94° were detected in all samples, which can be attributed to the CoS_2 (JCPDS 41−1471).[52−54] However, diffraction peaks at 2θ = 33.75° and 58.72° correspond to the (100) and (110) crystal planes of 2H−MoS_2 (JCPDS 37−1492),[52−54] respectively. The result is consistent with the FESEM images. When the reaction temperature rises to 200 °C, the intensity of the diffraction peaks associated with the CoS_2 crystal increases, while that attributed to the MoS_2 crystal is relatively constant. The results suggest that elevated temperatures promote the growth of the CoS_2 crystal, thereby improving its crystallinity. As the temperature reaches 220 °C, the (002) crystal plane of the MoS_2 was detected at 14.38°. It was consistent with the results of the EDS analysis (Figure 3). It is speculated that at 220 °C, $Co(NO_3)_2$ initially reacts with CH_4N_2S to form CoS_2, and subsequently, a reaction occurs between the residual CH_4N_2S and Na_2MoO_4 to produce MoS_2. The layered MoS_2 is deposited on the surface of polyhedral CoS_2 and forms a MoS_2-coated CoS_2 structure.

The microstructure of Co−MoS_2 ($Co(NO_3)_2$—0.6 g, 0.206 mol %) was further characterized by HRTEM, as illustrated in Figure 9. The Co−MoS_2 catalyst is composed of two kinds of textures, which is consistent with the morphology of the sample in FESEM. Figure 9b shows the HRTEM image (400,000×) of Co−MoS_2, indicating the composite has a densely packed edge. As calculated by software, the (002) lattice fringe spacing is 0.667 nm, which exceeds the theoretical lattice spacing of MoS_2 (0.615 nm), indicating the Co element was successfully doped into MoS_2. The lattice spacing of CoS_2 (0.248 nm) was observed in the HRTEM image (Figure 9c). As illustrated in Figure 9d, the distribution of the element Mo in the sample is uniform, as is the enrichment of the element Co in specific areas, and the cubic morphology of CoS_2 can also be observed. These observations are consistent with our initial hypotheses formulated. In addition, the crystallization properties of the CoS_2−MoS_2 composites have been investigated using SAED spectra (Figure 9e). The diffraction rings in Figure 9 (e) are indexed to the (002), (013) crystal planes of CoS_2 and the (002), (011) crystal planes of MoS_2, respectively, indicating that they are polycrystalline.

https://doi.org/10.1021/acsomega.4c10747
ACS Omega 2025, 10, 15129−15142

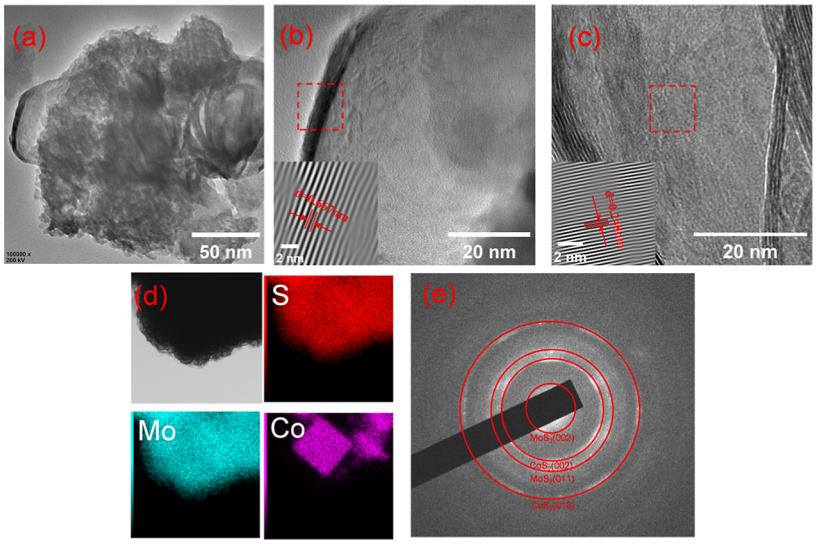

Figure 9. (a) HRTEM image of Co−MoS_2($Co(NO_3)_2$—0.6 g, 0.206 mol %), (b) TEM and HRTEM image of MoS_2 nanosheets, (c) TEM and HRTEM image of CoS_2 , (d) EDS elemental mapping of S, Mo, Co, (e) corresponding SAED pattern of Co−MoS_2($Co(NO_3)_2$—0.6 g, 0.206 mol %).

Figure 10 shows the XRD patterns of Co-doped MoS_2 with varying amounts. The XRD pattern of pristine MoS_2 exhibits

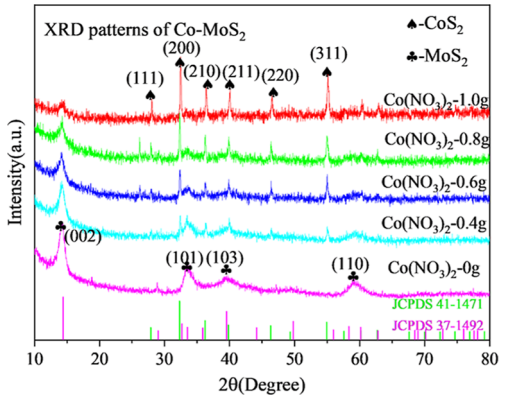

Figure 10. XRD patterns of Co-doped MoS_2 prepared with different $Co(NO_3)_2$ additions.

diffraction peaks at 2θ = 14.38°, 33.51°, 39.4° and 59.38°, which correspond to the (002), (100), (103), and (110) (JCPDS 37−1492)[52−54] crystal planes of 2H−MoS_2, respectively. With the increase of $Co(NO_3)_2$ addition amount, the diffraction peak of the (002) crystal plane exhibits a shift to the lower degree while the intensity of the peak decreases compared with pristine MoS_2. The position of the peak shift slightly to a lower angle may be caused by the introducing of the Co element into the MoS_2 matrix. The radius of the Co atom is smaller than that of the Mo atom, and the substitution of the Co atom reduces the thickness of the S−Mo−S structural unit, thus expanding the lattice spacing.[55] According to Bragg's law ($2d\sin\theta = n\lambda$), enlarged lattice spacing results in the peak position shift to a lower degree. When the $Co(NO_3)_2$ addition is 0.4 g(0.137 mol %), diffraction peaks located at 2θ = 27.88°, 32.30°, 36.24°, 39.83°, 46.32°, and 54.94°, which were assigned to the (111), (200), (210), (211), (220), and (311) crystal planes of CoS_2 (JCPDS 41−1471),[52−54] respectively, indicated CoS_2 was formed during the hydrothermal synthesis process of Co−MoS_2. However, the weak intensity of the diffraction peaks suggests poor crystallinity. As shown in Figure 10, with a higher doping addition of $Co(NO_3)_2$, the intensity of diffraction peaks enhanced, indicating more CoS_2 is formed. According to previous studies,[56,57] the reaction mechanism can be speculated as follows. Sodium molybdate is initially dissolved in water, forming molybdate ions (MoO_4^{2-}) (Reaction 2), in which Mo is in the +6 oxidation state, while cobalt nitrate forms Co^{2+} (Reaction 3). Subsequently, during the hydrothermal process, thiourea is dissolved in water to form NH_3 and H_2S (Reaction 4), which further decomposed to S^{2-} (Reaction 5). Then the NH_3 reacts with Co^{2+} from the cobalt source, forming a $[Co(NH_3)_4]^{2+}$ complex (Reaction 6). Following, a reaction between the $[Co(NH_3)_4]^{2+}$ complex and S^{2-} produced by thiourea occurs (Reaction 7) to form CoS_2. Finally, the residual sulfur reacted with MoO_4^{2-} and MoS_2 is formed (Reaction 8). Based on the reaction mechanism above, CoS_2 is preferentially synthesized. In this reaction, CH_4N_2S acts as both a reductant and the source of sulfur. The synthesis

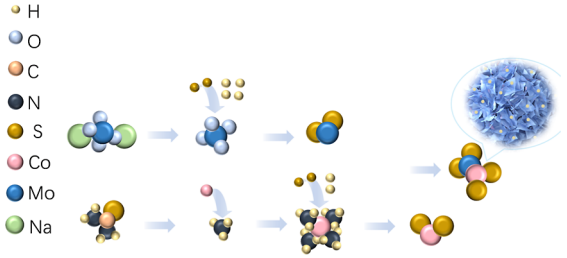

Figure 11. Synthesis mechanism of Co-doped MoS_2.

mechanism is shown in Figure 11 and the reaction equations are as follows

$$Na_2MoO_4 \rightarrow MoO_4^{2-} + 2Na^+ \quad (2)$$

$$Co(NO_3)_2 \rightarrow 2NO_3^- + Co^{2+} \quad (3)$$

$$SC(NH_2)_2 + 2H_2O \rightarrow 2NH_3 + H_2S + CO_2 \quad (4)$$

https://doi.org/10.1021/acsomega.4c10747
ACS Omega 2025, 10, 15129−15142

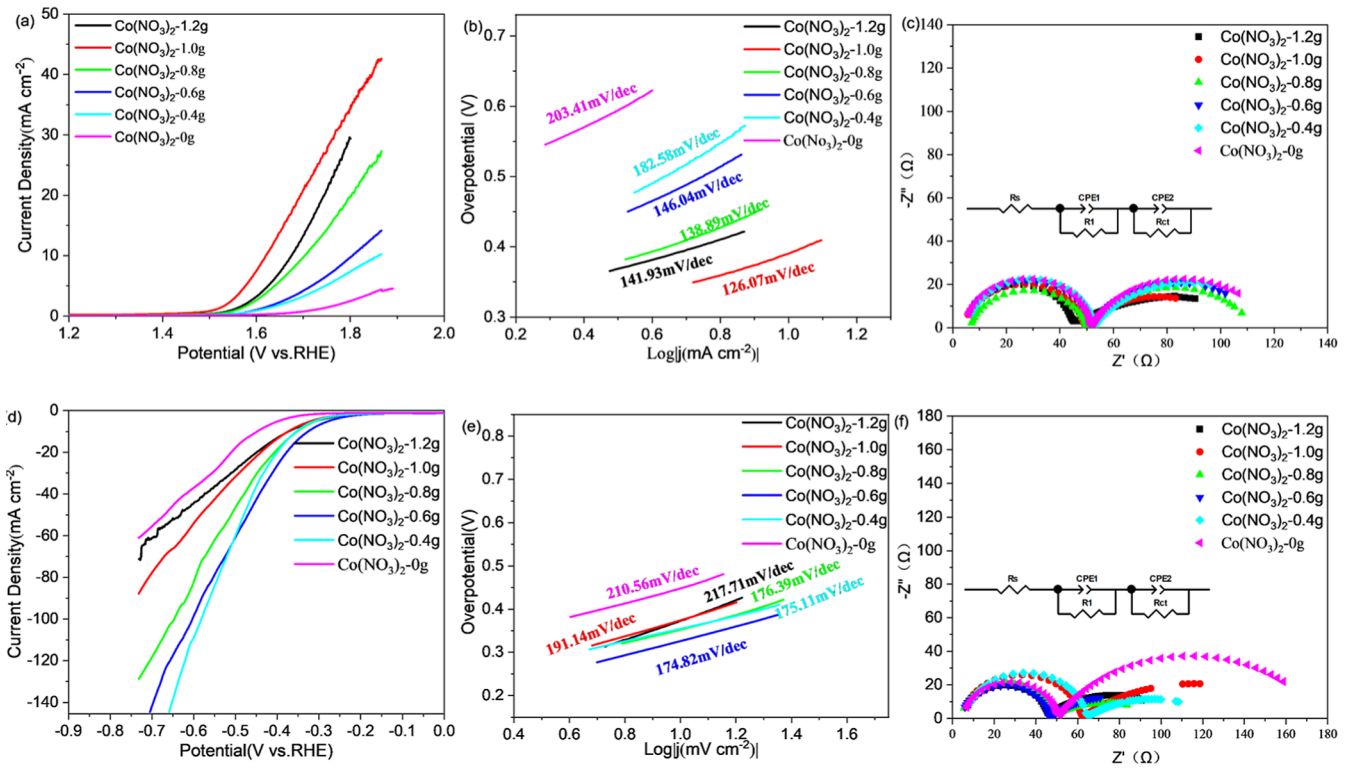

Figure 12. Bifunctional catalytic performance of MoS_2 prepared with different $Co(NO_3)_2$ additions: (a) LSV curve of OER, (b)Tafel plots of OER, (c) Nyquist plots of OER, (d) LSV curve of HER, (e) Tafel plots of HER, (f) Nyquist plots of HER.

$$H_2S \rightarrow 2H^+ + S^{2-} \quad (5)$$

$$Co^{2+} + 4NH_3 \rightarrow [Co(NH_3)_4]^{2+} \quad (6)$$

$$[Co(NH_3)_4]^{2+} + 2S^{2-} + 2H^+ \rightarrow CoS_2 + 4NH_3 + H_2 \quad (7)$$

$$4MoO_4^{2-} + 9S^{2-} + 24H^+ \rightarrow 4MoS_2 + SO_4^{2-} + 12H_2O \quad (8)$$

3.3. Bifunctional Catalytic Performance. The HER and OER performances of as-prepared MoS_2 with varying $Co(NO_3)_2$ additive amounts were tested in 0.1 M KOH. The LSV curve of the OER performance is presented in Figure 12a. As the quantity of $Co(NO_3)_2$ increased, the overpotential of the catalyst decreased gradually. The overpotential of samples with Co addition amounts of 0.4 g (0.137 mol %), 0.6 g (0.206 mol %), 0.8 g (0.274 mol %), and 1.0 g (0.343 mol %) at 10 mA cm^{-2} current density are 620 mV, 570 mV, 470 mV, and 444 mV, respectively. Without the Co element doping, the pristine MoS_2 exhibits a relatively low current density of less than 10 mA cm^{-2}, even at the maximum potential test in this study. In contrast, the sample with a doping amount of 1.0 g (0.343 mol %) has a minimum overpotential of 390 mV that attains the current density of 10 mA cm^{-2} (Figure 12a). As discussed in Section 3.1, CoS_2 has remarkable OER performance due to its distinct characteristics. On the other hand, the enhanced performance can be attributed to the partial Mo atoms coordinated with the S atom in the interlayer of MoS_2 being replaced by Co atoms. Based on this, S vacancies are further created to fully expose a large number of residual Mo atoms in the interlayer, thereby achieving the exposure of all potentially active sites of MoS_2[55]. The Tafel slope is employed to analyze the OER kinetics of the catalysts (Figure 12b). A smaller Tafel slope value generally represents superior OER kinetics. The Tafel slope of the catalyst with the $Co(NO_3)_2$ addition of 1.0 g (0.343 mol %) is 126.07 mV dec^{-1}, which is the smallest among all samples. With the increase of $Co(NO_3)_2$ addition, the catalytic activity of OER is more favorable. Figure 12c illustrates the EIS of the OER. The electron transfer efficiency at the interfaces between the material and electrolyte is assessed by charge transfer resistance (R_{ct}). Smaller R_{ct} values represent faster electron transfer, which means better electrocatalytic reaction kinetics. The R_{ct} value declines with the increasing doping amount of $Co(NO_3)_2$. Among all catalysts, the R_{ct} value of the sample with the $Co(NO_3)_2$ addition of 1.0 g is the lowest, which reflects the best interfacial catalytic reaction kinetics.

The HER activities of Co−MoS_2 and pristine MoS_2 counterpart in a 0.1 M KOH electrolyte were also explored (Figure 12d). Compared with pristine MoS_2, the specimens with cobalt addition all have a lower HER overpotential. The incorporation of the Co element enhances the conductivity of the catalyst, which leads to an improvement in the HER performance.[49] The specimen with the $Co(NO_3)_2$ doping amount of 0.6 g (0.206 mol %) exhibits a maximum decrease of overpotential by 130 mV, from 450 mV to 320 mV. Additionally, the Tafel slope was found to be the lowest, with a value of 174.82 mV dec^{-1}(Figure 12e), while the pristine MoS_2 exhibited 210.56 mV dec^{-1}. The results demonstrate that the as-prepared catalyst with $Co(NO_3)_2$ addition of 0.6 g (0.206 mol %) has an optimal synergistic effect between CoS_2 and MoS_2. The doping of the Co element will affect the state of Mo atoms, which in turn affects the electrocatalytic performance. However, the appropriate doping amount of the Co element, between 0.4 g (0.137 mol %) and 0.6 g (0.206 mol %), can extremely reduce the electron concentration of the S atom on

https://doi.org/10.1021/acsomega.4c10747
ACS Omega 2025, 10, 15129−15142

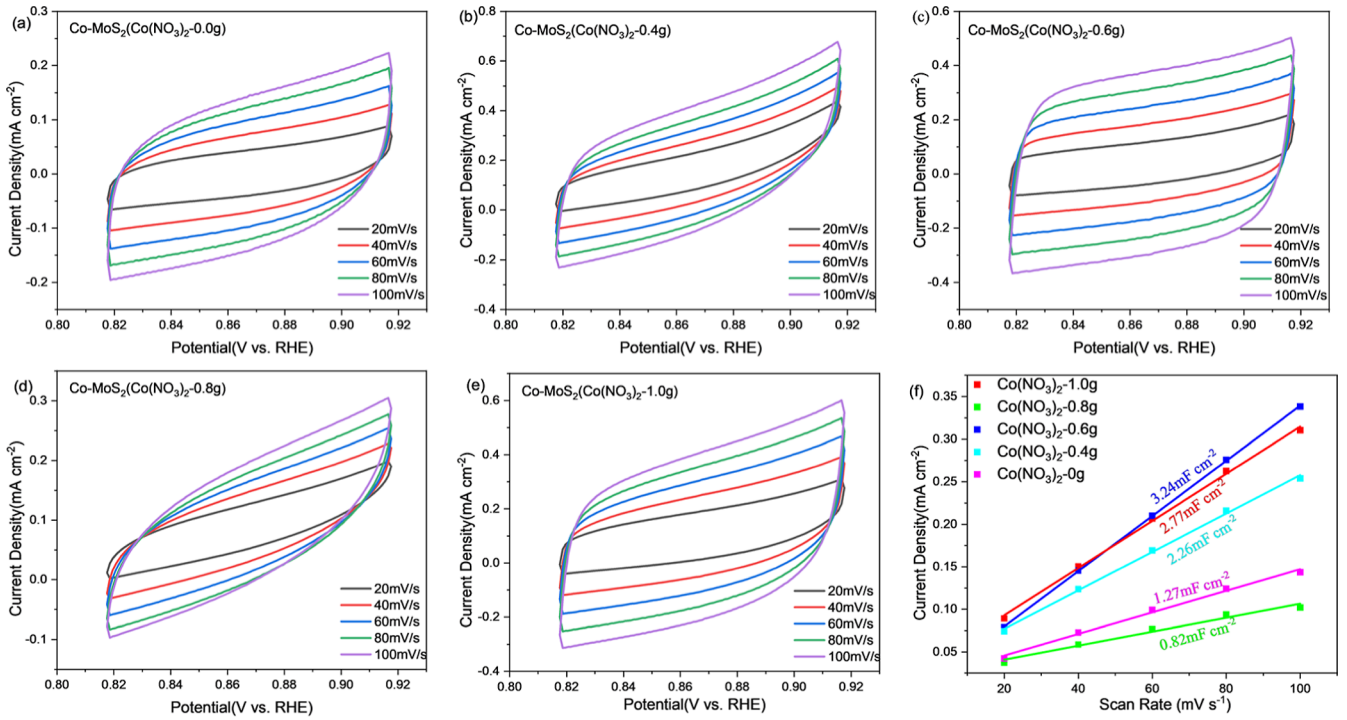

Figure 13. (a-e) CV curves of Co−MoS_2 prepared with different $Co(NO_3)_2$ additions in the non-Faraday capacitance current range. (f) C_{dl} of various as-prepared catalysts.

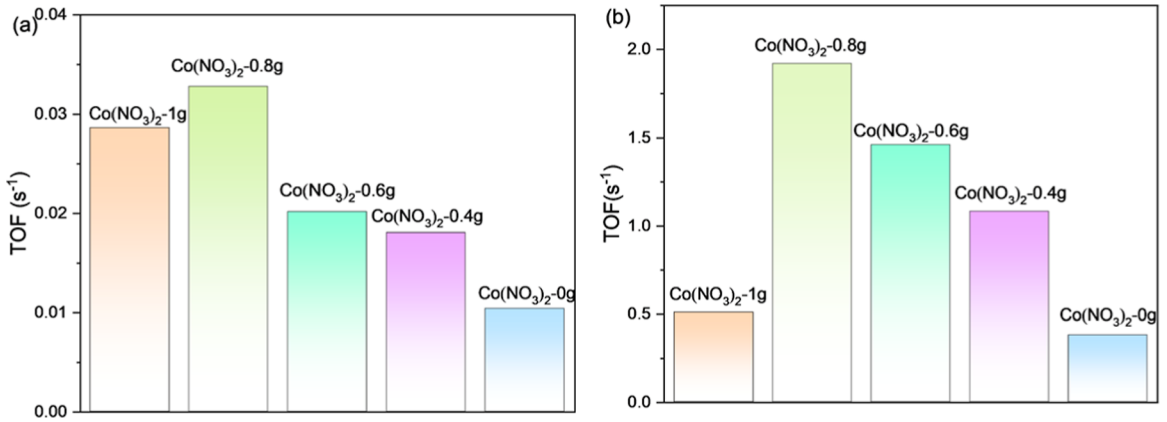

Figure 14. TOF values of MoS_2 prepared with different $Co(NO_3)_2$ additions: (a) at the overpotential of 270 mV for OER, (b) at the overpotential of 350 mV for HER.

the surface, thereby enhancing the adsorption of H*. The catalysts can exhibit the maximum HER catalytic activity when the $Co(NO_3)_2$ addition is within the range above. In contrast, excessive doping leads to excessive H* adsorption, resulting in difficulty in the subsequent desorption of H_2.[58] The crystal growth and crystallinity of MoS_2 will also be affected, resulting in a decline in the HER catalytic activity. To further explore the efficient HER kinetics of the Co−MoS_2, EIS analysis was performed. As illustrated in Figure 12f, it was observed that the Co−MoS_2 catalyst, with the $Co(NO_3)_2$ addition amount of 0.6 g (0.206 mol %), exhibited the smallest semicircle diameter among all the as-prepared samples, indicating that the catalyst has the smallest charge transfer resistance compared to the other catalysts.

Figure 13 (a-e) illustrates the CV curves of varying $Co(NO_3)_2$ addition amounts of Co−MoS_2. The values of C_{dl} were calculated from the CV curves illustrated in Figure 13f. The sample with a $Co(NO_3)_2$ doping amount of 0.6 g (0.206 mol %) exhibited the maximum C_{dl}, which is superior to those of other as-prepared catalysts. A higher value of C_{dl} indicates that the catalyst possesses a larger ECSA. Also, it indicates that the active surface area is more exposed and fully utilized for the reaction.

The turnover frequency (TOF) is an important parameter for quantitative HER activity and can reflect the intrinsic activity of the electrocatalysts. The computational formula for turnover frequency (TOF) is $TOF = \frac{j \times A \times C}{* \times A}$ and based on previous reports,[59−61] where C, j, A, and * represent the turnover event, the current density at specific overpotential, the geometric area of the catalyst, and the number of active sites per unit area. Here, C is 3.12×10^{15} s^{-1} cm^{-2} per mA cm^{-2} for HER and 1.56×10^{15} s^{-1} cm^{-2} per mA cm^{-2} for OER, and A is 0.196 cm^2. For all materials, a reasonable approximation of

https://doi.org/10.1021/acsomega.4c10747
ACS Omega 2025, 10, 15129−15142

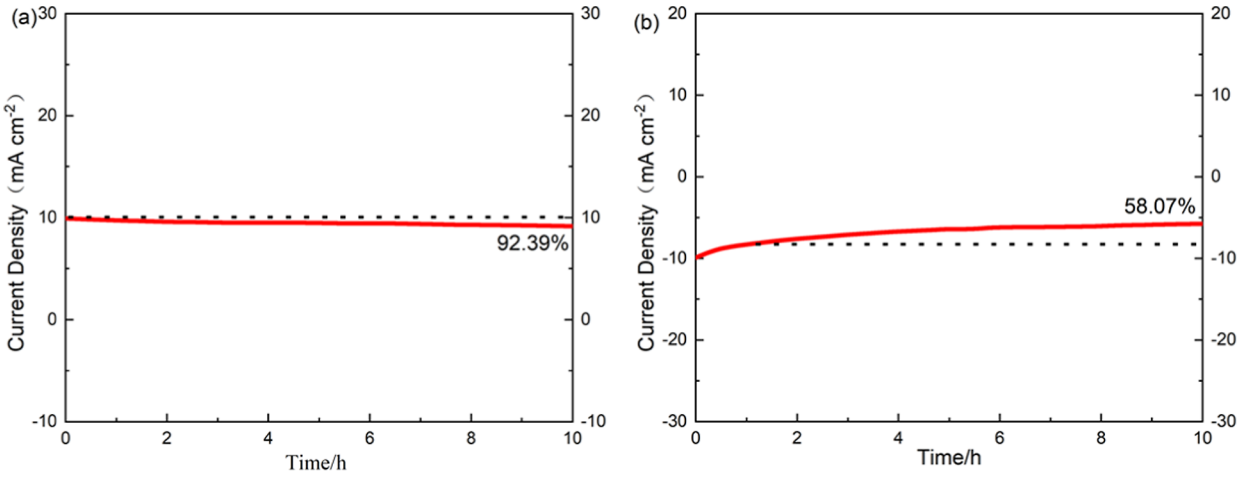

Figure 15. *i-t* curves of the Co−MoS_2 catalyst in 0.1 M KOH: (a) OER, (b) HER.

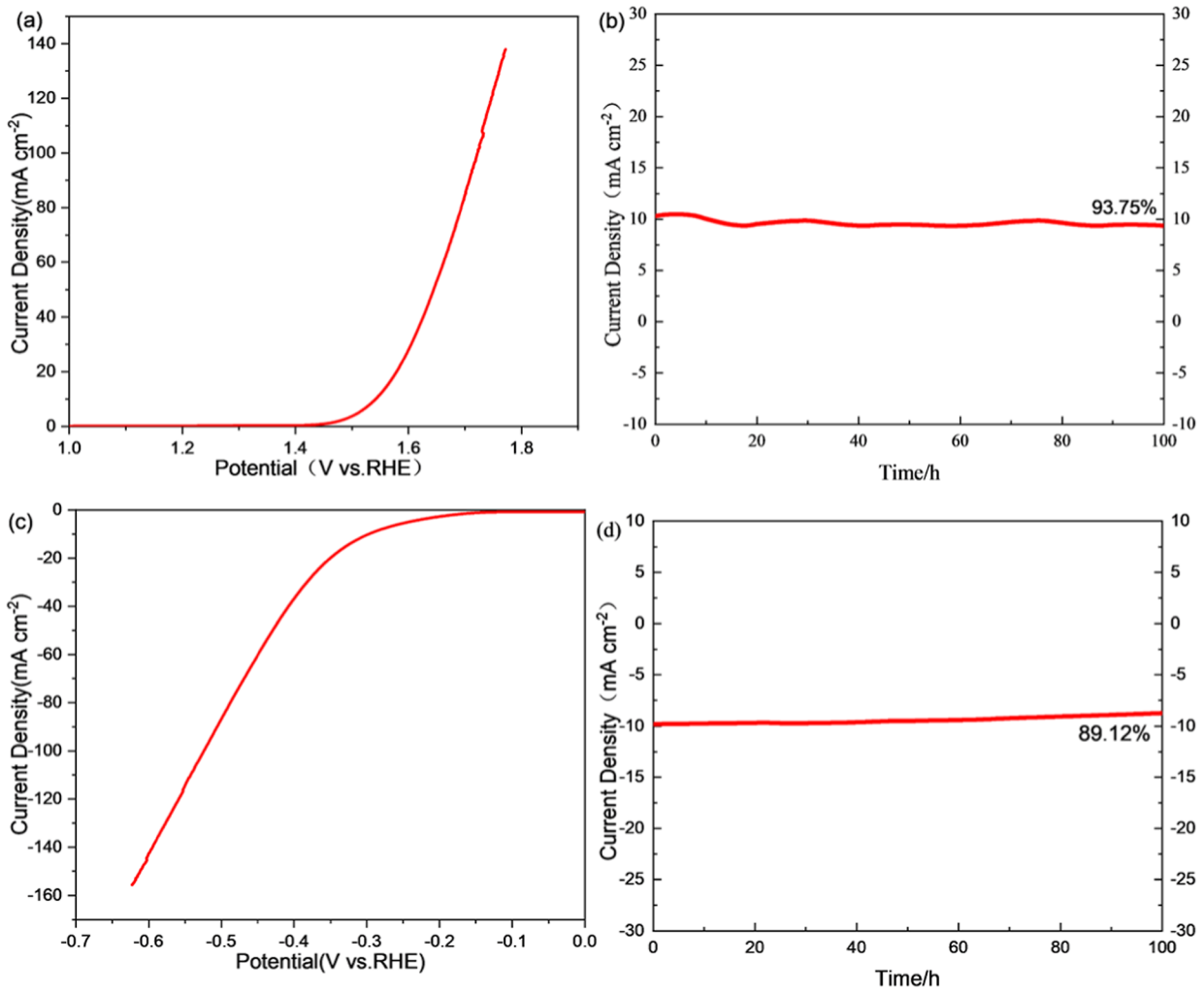

Figure 16. Electrocatalytic performance of the Co−MoS_2 catalyst in 1 M KOH: (a) LSV curve of OER, (b) *i-t* curve of OER, (c) LSV curve of HER, (d) *i-t* curve of HER.

surface site density is close to 10^{15} cm^{-2}. Thus, * is calculated by $N = C_{dl}/C_s \times 10^{15}$ cm^{-2}.

TOF values can reflect the intrinsic activity of the electrocatalysts. As shown in Figure 14a, the TOF values Co−MoS_2 ($Co(NO_3)_2$—0 g, 0 mol %), Co−MoS_2 ($Co(NO_3)_2$—0.4 g, 0.137 mol %), Co−MoS_2 ($Co(NO_3)_2$—0.6 g, 0.206 mol %), Co−MoS_2 ($Co(NO_3)_2$—0.8 g, 0.274 mol %), and Co−MoS_2 ($Co(NO_3)_2$—1.0 g, 0.343 mol %) at the overpotential of 270 mV are 0.0104, 0.0181, 0.0202, 0.0328, and 0.0287 s^{-1} in the process of OER, respectively. The TOF values demonstrate that Co−MoS_2 ($Co(NO_3)_2$—0.8 g, 0.274 mol %) exhibits the optimal intrinsic catalytic activity for OER.

https://doi.org/10.1021/acsomega.4c10747
ACS Omega 2025, 10, 15129−15142

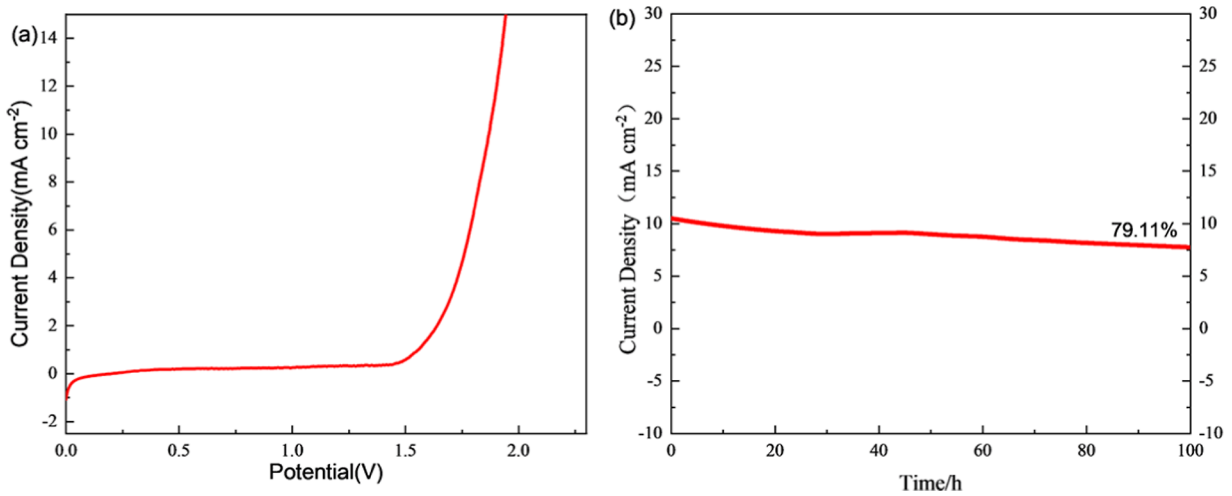

Figure 17. Overall water splitting performance of the Co−MoS_2 catalyst: (a) LSV curve in 1 M KOH, (b) *i-t* curve in 1 M KOH.

Figure 14b illustrates the TOF values of Co−MoS_2 (Co-$(NO_3)_2$—0 g, 0 mol %), Co−MoS_2 ($Co(NO_3)_2$—0.4 g, 0.137 mol %), Co−MoS_2 ($Co(NO_3)_2$—0.6 g, 0.206 mol %), Co−MoS_2 ($Co(NO_3)_2$—0.8 g, 0.274 mol %), and Co−MoS_2 ($Co(NO_3)_2$—1.0 g, 0.343 mol %) at the overpotential of 350 mV are 0.3804, 1.0809, 1.4602, 1.4832, 1.9197, and 0.5084 s^{-1}, respectively. The TOF values demonstrate that Co−MoS_2 ($Co(NO_3)_2$—0.8 g, 0.274 mol %) exhibits the optimal intrinsic catalytic activity for HER. Turnover frequency (TOF) reflects the number of reactions per unit active site per unit time of the catalyst. A higher TOF value is indicative of high catalytic activity, implying that the catalyst can promote the reaction at an accelerated rate. However, it is imperative to consider energy consumption as an integral component in the evaluation of catalyst performance. However, a high TOF value indicates a rapid reaction rate, if the energy consumption is excessive, the overall efficiency will be diminished.

The cycle stability of the samples with the $Co(NO_3)_2$ addition of 0.6 g (0.206 mol %) was evaluated by *i-t* testing(Figure 15) at a constant potential of 0.57 V and −0.32 V (vs RHE) for OER and HER, respectively. The current density in Figure 15 exhibits a decreasing tendency, but it still maintains a relatively high current density after 10 h of reactions, indicating the $Co(NO_3)_2$ doping amount of 0.6 g (0.206 mol %) possesses feasible stability characteristics in 0.1 M KOH. It is conceivable that the combination of MoS_2 and CoS_2 may result in structural alternation and modifications to the electronic configuration, facilitating electron transfer between the catalyst surface and the reaction intermediate. This could potentially enhance the electrocatalytic performance and stability.

Subsequently, a typical three-electrode system measured the electrocatalytic performance of Co−MoS_2 ($Co(NO_3)_2$—0.6 g, 0.206 mol %) in 1 M KOH electrolyte. From the LSV curve (Figure 16a,c), it can be seen that the overpotential was significantly improved compared to 0.1 M KOH. At a current density of 10 mA cm^{-2}, the overpotentials for OER and HER of Co−MoS_2 ($Co(NO_3)_2$—0.6 g, 0.206 mol %) are 312 mV and 297 mV, respectively. In addition, an assessment of the stability was carried out. It was evaluated by a continuous constant voltage (*i-t*) test at 0.31 V vs RHE and −0.30 V vs RHE, respectively, for OER and HER. According to Figure 16b, and 16d, the current density exhibits a gradually decreasing tendency. After 100 h of reaction, the current density of OER and HER remained at 93.75% and 89.12%, respectively, indicating that Co−MoS_2 ($Co(NO_3)_2$—0.6 g, 0.206 mol %) displays remarkable durability.

As a water-splitting catalyst with excellent OER and HER performance, Co−MoS_2 ($Co(NO_3)_2$—0.6 g, 0.206 mol %) was used as the electrode of the cathode and anode to construct an alkaline water-splitting device with 1 M KOH as the electrolyte. As illustrated in Figure 17a, Co−MoS_2 ($Co(NO_3)_2$—0.6 g, 0.206 mol %) requires 1.87 V to reach a current density of 10 mA cm^{-2} in the reaction of 1 M KOH electrolyte. The durability of the catalyst was investigated at 10 mA cm^{-2} in 1 M KOH. It has been demonstrated to operate stably at a current density of 10 mA·cm^{-2} for more than 100 h with a current density decay of 20.89% in a 1.0 M KOH solution (Figure 17b).

Furthermore, in order to explore the morphological changes of the catalyst after the stability testing, samples were collected after OER and HER processes, and FESEM and TEM images were obtained. The observation of the FESEM and TEM images reveals that for Co−MoS_2 ($Co(NO_3)_2$—0.6 g, 0.206 mol %) after 100 h of the OER process, the morphology of the sample changes from nanoflowers to the coexistence of blocks and flakes, as illustrated in Figure S4(a). Due to long-term test conditions, physical reconstruction or aggregation may occur, resulting in block and sheet structures. The chemical substances (such as oxygen, etc.) that may exist in the test environment may react with the sample, resulting in a change in morphology. This kind of effect may promote the agglomeration or rearrangement of nanoparticles. Through the TEM image and elements mapping (Figure S4(b), and (c)), it can be obtained that after 100 h of OER, CoS_2 is separated from the external MoS_2. The exposed CoS_2 has superior OER performance, ensuring relatively good OER stability during the catalytic process.

Accordingly, Figure S5 illustrates morphological changes of the catalyst after the HER reaction. As depicted in Figure S5(a), it reveals that the specimen undergoes a transformation from its initial nanoflower configuration to a sheet-like stacked morphology during the HER. The TEM image and elements mapping (Figure S5(b), (c)) reveal that, despite the alterations in microscopic morphology, the composition remains MoS_2 wrapped on CoS_2. The distribution of cobalt elements is

https://doi.org/10.1021/acsomega.4c10747
ACS Omega 2025, 10, 15129−15142

predominantly located within the interior, while the periphery consists of molybdenum disulfide. Studies have shown that MoS_2 has excellent HER performance, but most of the sites on its exposed surface are inert. Although the periphery is still mainly composed of MoS_2, its stability decreased by 10.88%, and relatively high stability is maintained.

4. CONCLUSIONS

In this work, Co-doping into MoS_2 bifunctional catalysts for water splitting was prepared via a one-step hydrothermal process. The influence of reaction temperature and the addition of $Co(NO_3)_2$ on the structure characteristics and catalytic activity of MoS_2 were investigated. Elevated synthesis temperature is beneficial to the preparation of samples with excellent catalytic performance. The Co−MoS_2 composite obtained through a hydrothermal process of 220 °C exhibits a composite structure with polyhedral CoS_2 as the substrate and MoS_2 nanoflower as the coating layer. As the $Co(NO_3)_2$ addition amount increased, the peak intensity of the CoS_2 phase enhanced while that of MoS_2 was decreased. The introduction of CoS_2 led to a remarkable enhancement in the catalytic activity of OER. At a current density of 10 mA cm^{-2}, the overpotential decreased with the increasing doping amount of $Co(NO_3)_2$. However, the HER catalytic activity initially increased followed by a subsequent decline. At the current density of 10 mA cm^{-2}, the minimum overpotential was observed to be 320 mV for HER, and the OER was also extremely reduced when 0.6 g of $Co(NO_3)_2$ was added. 312 mV and 297 mV are required to achieve the current density of 10 mA cm^{-2} in 1 M KOH electrolyte. It was found that a voltage of 1.869 V was sufficient to reach a current density of 10 mA cm^{-2} in 1 M KOH. The results of the stability analysis indicate that the sample exhibits better stability, and this phenomenon may be attributable to the incorporation of CoS_2 and MoS_2.

■ ASSOCIATED CONTENT

Supporting Information

The Supporting Information is available free of charge. LSV curves before and after 1000 CV cycles; LSV curves of Co_3S_4−MoS_2 in 0.1 M KOH; FESEM images and elemental mapping of Co−MoS_2($Co(NO_3)_2$—0.6 g, 0.206 mol %); FESEM image, TEM image and EDS elemental mapping of Co−MoS_2($Co(NO_3)_2$—0.6 g, 0.206 mol %) after OER; FESEM image, TEM image and EDS elemental mapping of Co−MoS_2($Co(NO_3)_2$—0.6 g, 0.206 mol %) after HER; comparison of OER performances of Co−MoS_2($Co(NO_3)_2$—0.6 g) with noble-metal free electrocatalysts at 10 mA cm^{-2} in 1.0 M KOH; and comparison of HER performances of Co−MoS_2($Co(NO_3)_2$—0.6 g) with noble-metal free electrocatalysts at 10 mA cm^{-2} in 1.0 M KOH (PDF) The Supporting Information is available free of charge at https://pubs.acs.org/doi/10.1021/acsomega.4c10747.

(PDF)

■ AUTHOR INFORMATION

Corresponding Author

Wei Liu − *School of Material Science and Engineering, Henan University of Science and Technology, Luoyang 471003, China; Henan University of Science and Technology National Joint Engineering, Research Center for Abrasion Control and Molding of Metal Materials, Luoyang 471023, China;* orcid.org/0009-0003-0773-201X; Email: liuwei@haust.edu.cn

Authors

Linping Fu − *School of Material Science and Engineering, Henan University of Science and Technology, Luoyang 471003, China; Henan University of Science and Technology National Joint Engineering, Research Center for Abrasion Control and Molding of Metal Materials, Luoyang 471023, China*

Shenshen Yang − *School of Material Science and Engineering, Henan University of Science and Technology, Luoyang 471003, China; Henan University of Science and Technology National Joint Engineering, Research Center for Abrasion Control and Molding of Metal Materials, Luoyang 471023, China*

Yaozong Lu − *School of Material Science and Engineering, Henan University of Science and Technology, Luoyang 471003, China; Henan University of Science and Technology National Joint Engineering, Research Center for Abrasion Control and Molding of Metal Materials, Luoyang 471023, China*

Ming Li − *School of Material Science and Engineering, Henan University of Science and Technology, Luoyang 471003, China*

Longhua Zhang − *School of Material Science and Engineering, Henan University of Science and Technology, Luoyang 471003, China*

Jiaqi Tang − *School of Material Science and Engineering, Henan University of Science and Technology, Luoyang 471003, China*

Complete contact information is available at: https://pubs.acs.org/10.1021/acsomega.4c10747

Notes

The authors declare no competing financial interest.

■ ACKNOWLEDGMENTS

This work is supported by the National Natural Science Foundation of China (no. U1404511), Henan Province Science and Technology R&D Program Joint Fund Project (no.222103810038), Student Research Training Program of Henan University of Science and Technology (no.2024049), Henan Provincial University Key Research Project (no.24B430007), and the Collaborative Innovation Center for New Materials and Advanced Processing Technologies of Nonferrous Metals.

■ REFERENCES

(1) Yu, H.; Xie, S.; Yang, J.; Lv, J.; Tan, W.; Yin, J.; Wang, J.; Zhao, M.; Wang, C.; Zhang, M.; et al. Co_3Fe_7/Mo_2C co-embedded in N-codoped porous carbon with accelerated kinetics for OER and HER. *Colloids Surf., A* **2022**, *645*, 128953.

(2) Liu, J.; Huang, Z.; Fan, M.; Yang, J.; Xiao, J.; Wang, Y. Future Energy Infrastructure, Energy Platform and Energy Storage. *Nano Energy* **2022**, *104*, 107915.

(3) Li, S.; Bai, L.; Shi, H.; Hao, X.; Chen, L.; Qin, X.; Shao, G. Mo-doped CoP nanosheets as high-performance electrocatalyst for HER and OER. *Ionics* **2021**, *27* (7), 3109−3118.

(4) Sun, H.; Yu, S.; Yin, J.; Li, J.; Yu, J.; Liu, T.; Liang, W.; Zhang, N.; Zhang, Y.; Ye, C.; Hu, M.; Du, Y. Ir Doping Modulates the Electronic Structure of Flower-Shaped Phosphides for Water Oxidation. *Inorg. Chem.* **2024**, *63* (44), 21283−21292.

(5) Yu, J.; Wang, X.; Zhang, Y.; Liu, T.; Wu, Z.; Yu, S.; Du, Y. Structural optimization: Ternary FeNiZn sulfide nanoparticles anchored on nanosheets to strengthen oxygen evolution reaction. *Int. J. Hydrogen Energy* **2024**, *82*, 359−366.
(6) Yu, S.; Li, J.; Du, Y.; Wang, Y.; Zhang, Y.; Wu, Z. Sulfur-modified MOFs as efficient electrocatalysts for overall water splitting. *Coord. Chem. Rev.* **2024**, *520*, 216144.
(7) Singha Roy, S.; Karmakar, A.; Madhu, R.; Nagappan, S.; N Dhandapani, H.; Kundu, S. Three-Dimensional Sm-Doped NiCu-LDH on Ni Foam as a Highly Robust Bifunctional Electrocatalyst for Total Water Splitting. *ACS Appl. Energy Mater.* **2023**, *6* (17), 8818−8829.
(8) Singha Roy, S.; Madhu, R.; Bera, K.; Nagappan, S.; Dhandapani, H. N.; De, A.; Kundu, S. Tuning the activity and stability of CoCr-LDH by forming a heterostructure on surface-oxidized nickel foam for enhanced water-splitting performance. *ACS Appl. Mater. Interfaces* **2024**, *16* (5), 5965−5976.
(9) Madhu, R.; Kundu, S. Unlocking the potential of NiV-LDH@ Mn 2 O 3 heterostructure via band gap modulation for enhanced water splitting. *J. Mater. Chem. A* **2024**, *12* (32), 21385−21397.
(10) Madhu, R.; Muthukumar, J.; Arunachalam, P.; Gudlur, P.; Kundu, S. Unraveling Activation Energy with Temperature-Dependent Analyses of CoNiSe2 Electrocatalysts Derived from CoNi-LDH for Water Splitting Reaction. *J. Phys. Chem. C* **2024**, *128* (31), 12891−12902.
(11) Zou, X.; Zhang, Y. Noble metal-free hydrogen evolution catalysts for water splitting. *Chem. Soc. Rev.* **2015**, *44* (15), 5148−5180.
(12) Zhang, T.; Zhang, B.; Peng, Q.; Zhou, J.; Sun, Z. Mo_2B_2 MBene-supported single-atom catalysts as bifunctional HER/OER and OER/ORR electrocatalysts. *J. Mater. Chem.* **2021**, *9* (1), 433−441.
(13) Li, S.; Luo, Z.; Wang, S.; Cheng, H. Atomic structure and HER performance of doped MoS_2: A mini-review. *Electrochem. Commun.* **2023**, *155*, 107563.
(14) Wang, J.; Hu, Y.; Wang, F.; Yan, Y.; Chen, Y.; Shao, M.; Wu, Q.; Zhu, S.; Diao, G.; Chen, M. Development of copper foam-based composite catalysts for electrolysis of water and beyond. *Sustainable Energy & Fuels* **2023**, *7* (7), 1604−1626.
(15) Shiqing, D. *Doping modulation and synchrotron radiation characterization of water splitting electrocatalysts*; University of Science and Technology of China, 2021.
(16) Karmakar, A.; Durairaj, M.; Madhu, R.; De, A.; Dhandapani, H. N.; Spencer, M. J.; Kundu, S. From Proximity to Energetics: Unveiling the Hidden Compass of Hydrogen Evolution Reaction. *ACS Mater. Lett.* **2024**, *6*, 3050−3062.
(17) Yu, S.; Li, J.; Yin, J.; Liang, W.; Zhang, Y.; Liu, T.; Hu, M.; Wang, Y.; Wu, Z.; Zhang, Y.; et al. Built-in electric field and core-shell structure of the reconstructed sulfide heterojunction accelerated water splitting. *Chin. Chem. Lett.* **2024**, *35*, 110068.
(18) Li, T.; Li, S.; Liu, Q.; Yin, J.; Sun, D.; Zhang, M.; Xu, L.; Tang, Y.; Zhang, Y. Immobilization of Ni_3Co Nanoparticles into N-Doped Carbon Nanotube/Nanofiber Integrated Hierarchically Branched Architectures toward Efficient Overall Water Splitting. *Advanced science (Weinheim, Baden-Wurttemberg, Germany)* **2020**, *7* (1), 1902371.
(19) Zhao, L.; Liu, S.; Wei, L.; He, H.; Jiang, B.; Zhan, Z.; Wang, J.; Li, X.; Gou, W. One-pot Hydrothermal Synthesis of Bifunctional Co/Mo-rGO efficient Electrocatalyst for HER/OER in Water Splitting. *Catal. Lett.* **2024**, *154*, 5294−5302.
(20) Saddeler, S.; Hagemann, U.; Bendt, G.; Schulz, S. Core-shell Co_3O_4@CoO Nanoparticles for Enhanced OER Activity. *ChemCatChem* **2024**, *16* (6), No. e202301327.
(21) Chen, B.; Hu, P.; Yang, F.; Hua, X.; Yang, F. F.; Zhu, F.; Sun, R.; Hao, K.; Wang, K.; Yin, Z. In Situ Porousized MoS_2 Nano Islands Enhance HER/OER Bifunctional Electrocatalysis. *Small* **2023**, *19* (14), 2207177.
(22) Hou, X.; Xie, K.; Huang, Z.; Shi, C.; Wei, Q.; Hu, Y. Co-MOF induced "blossom branch like" MoS_2@Co_9S_8/C nanofibers as a bifunctional catalyst for HER and OER. *Appl. Surf. Sci.* **2023**, *616*, 156486.
(23) Wang, H.; Zhang, C.; Zhang, D.; Jiang, L.; Gao, Y.; Zhuang, T.; Lv, Z. I Single-Atom Doped P-Rich CoPn Nanocluster@CoP with Enhanced HER. *Small* **2024**, *19* (14), 2207177.
(24) Lin, Y.; Cui, X.; Zhao, Y.; Liu, Z.; Zhang, G.; Pan, Y. Heterojunction interface editing in Co/NiCoP nanospheres by oxygen atoms decoration for synergistic accelerating hydrogen and oxygen evolution electrocatalysis. *Nano Res.* **2023**, *16* (7), 8765−8772.
(25) Peng, L.; Shah, S. S. A.; Wei, Z. Recent developments in metal phosphide and sulfide electrocatalysts for oxygen evolution reaction. *Chin. J. Catal.* **2018**, *39* (10), 1575−1593.
(26) Hinnemann, B.; Moses, P. G.; Bonde, J.; Jørgensen, K. P.; Nielsen, J. H.; Horch, S.; Chorkendorff, I.; Nørskov, J. K. Biomimetic Hydrogen Evolution: MoS2 Nanoparticles as Catalyst for Hydrogen Evolution. *J. Am. Chem. Soc.* **2005**, *127* (15), 5308−5309.
(27) Wang, X.; Zhang, Y.; Si, H.; Zhang, Q.; Wu, J.; Gao, L.; Wei, X.; Sun, Y.; Liao, Q.; Zhang, Z.; et al. Single-atom vacancy defect to trigger high-efficiency hydrogen evolution of MoS_2. *J. Am. Chem. Soc.* **2020**, *142* (9), 4298−4308.
(28) Zhao, X.; He, D.; Xia, B. Y.; Sun, Y.; You, B. Ambient Electrosynthesis toward Single-Atom Sites for Electrocatalytic Green Hydrogen Cycling. *Adv. Mater.* **2023**, *35* (14), 2210703.
(29) Qiu, X.; Huang, Y.; Nie, Z.; Ma, B.; Tan, Y.; Wu, Z.; Zhang, N.; Xie, X. Support interactions dictated active edge sites over MoS_2-carbon composites for hydrogen evolution. *Nanoscale* **2020**, *12* (2), 1109−1117.
(30) Xu, X.; Xu, W.; Zhang, L.; Liu, G.; Wang, X.; Zhong, W.; Du, Y. Interface engineering heterostructured MoS_2/WS_2-reduced graphene Oxide for enhanced hydrogen Evolution electrocatalysts. *Sep. Purif. Technol.* **2021**, *278*, 119569.
(31) Li, Z.; Li, C.; Chen, J.; Xing, X.; Wang, Y.; Zhang, Y.; Yang, M.; Zhang, G. Confined synthesis of MoS_2 with rich co-doped edges for enhanced hydrogen evolution performance. *J. Energy Chem.* **2022**, *70*, 18−26.
(32) Munusamy, T. D.; Khan, M. R.; Chin, S. Y. Photo-electrochemical performance of P@ MoS_2 for hydrogen evolution reaction. *Mater. Today: Proc.* **2022**, *48*, 766−770.
(33) Wang, X.; Liu, Y.; Zhang, T.; Luo, Y.; Lan, Z.; Zhang, K.; Zuo, J.; Jiang, L.; Wang, R. Geometrical-Site-Dependent Catalytic Activity of Ordered Mesoporous Co-Based Spinel for Benzene Oxidation: In Situ DRIFTS Study Coupled with Raman and XAFS Spectroscopy. *ACS Catal.* **2017**, *7* (3), 1626−1636.
(34) Wang, T.; Zhuo, J.; Du, K.; Chen, B.; Zhu, Z.; Shao, Y.; Li, M. Electrochemically Fabricated Polypyrrole and MoS_x Copolymer Films as a Highly Active Hydrogen Evolution Electrocatalyst. *Adv. Mater.* **2014**, *22* (26), 3761−3766.
(35) Lin, Q. *Preparation of 2D Material Supported Cobalt-based Catalysts and Their Applications in Electrochemical Water Splitting*; Tianjin University, 2020.
(36) Ganesan, V.; Kim, J. Multi-shelled CoS_2−MoS_2 hollow spheres as efficient bifunctional electrocatalysts for overall water splitting. *Int. J. Hydrogen Energy* **2020**, *45* (24), 13290−13299.
(37) Zhipeng, L.; Kaiwen, W.; Yanjuan, L.; Shisheng, Y.; Guoqing, H.; Xiaotian, L.; Nan, L. Activation engineering on metallic 1T-MoS_2 by constructing In-plane heterostructure for efficient hydrogen generation. *Appl. Catal* **2021**, *300*, 120696.
(38) Mu, X.; Wang, K.; Lv, K.; Feng, B.; Yu, X.; Li, L.; Zhang, X.; Yang, X.; Lu, Z. Doping of Cr to Regulate the Valence State of Cu and Co Contributes to Efficient Water Splitting. *ACS Appl. Mater. Interface* **2023**, *15* (13), 16552−16561.
(39) Wang, T.; Chang, P.; Sun, Z.; Wang, X.; Tao, J.; Guan, L. Interface prompted highly efficient hydrogen evolution of MoS_2/CoS_2 heterostructures in a wide pH range. *Phys. Chem. Chem. Phys.* **2023**, *25* (20), 13966−13977.
(40) Chen, B.; Wang, J.; He, S.; Shen, Y.; Huang, S.; Zhou, H. Fabrication of CoS_2-MoS_2 heterostructure via interface engineering

https://doi.org/10.1021/acsomega.4c10747
ACS Omega 2025, 10, 15129−15142

toward efficient dual-pH hydrogen evolution. *J. Alloys Compd.* **2023**, *948*, 169655.
(41) Hou, X.; Zhou, H.; Zhao, M.; Cai, Y.; Wei, Q. MoS_2 Nanoplates Embedded in Co−N-Doped Carbon Nanocages as Efficient Catalyst for HER and OER. *ACS Sustain. Chem. Eng.* **2020**, *8* (14), 5724−5733.
(42) Wu, Y.; Zhang, L. L.; Wang, W.; Fan, D. S.; Yang, S. S.; Bai, Y. H.; Li, J. W.; Liu, W. Enhanced hydrothermal synthesis and electrochemical performance of subsphaeroidal MoS_2 used as anode material for lithium-ion batterie. *Rare Met. Mater. Eng.* **2023**, *52* (8), 2893−2900.
(43) Liu, W.; Yang, S.; Fan, D.; Wu, Y.; Zhang, J.; Lu, Y.; Fu, L. PEG−PVP-Assisted Hydrothermal Synthesis and Electrochemical Performance of N-Doped MoS_2/C Composites as Anode Material for Lithium-Ion Batteries. *ACS Omega* **2024**, *9* (8), 9792−9802.
(44) Ma, J.; Cai, A.; Guan, X.; Li, K.; Peng, W.; Fan, X.; Zhang, G.; Zhang, F.; Li, Y. Preparation of ultrathin molybdenum disulfide dispersed on graphene via cobalt doping: A bifunctional catalyst for hydrogen and oxygen evolution reaction. *Int. J. Hydrogen Energy* **2020**, *45* (16), 9583−9591.
(45) Cao, X.; Chen, Z.; Wang, N.; Han, Z.; Zheng, X.; Yang, R. J. E. A. Defected molybdenum disulfide catalyst engineered by nitrogen doping for advanced lithium-oxygen battery. *Electrochim. Acta* **2021**, *383*, 138369.
(46) Zhu, T.; Shen, W.; Wang, X.; Song, Y.-F.; Wang, W. Paramagnetic CoS_2@MoS2 core-shell composites coated by reduced graphene oxide as broadband and tunable high-performance microwave absorbers. *Chem. Eng. J.* **2019**, *378*, 122159.
(47) Zhouling, W. *Study on the Preparation and Electrochemical Properties of Cobalt-based Oxides for Oxygen Electrode*; Heilongjiang University, 2017.
(48) Huang, N.; Ding, Y.; Yan, S.; et al. Ultrathin MoS_2 Nanosheets Vertically Grown on CoS_2 Acicular Nanorod Arrays: A Synergistic Three-Dimensional Shell/Core Heterostructure for High-Efficiency Hydrogen Evolution at Full pH. *ACS Appl. Energy Mater.* **2019**, *2* (9), 6751−6760.
(49) Wu, J.; Chen, T.; Zhu, C.; Du, J.; Huang, L.; Yan, J.; Cai, D.; Guan, C.; Pan, C. Rational Construction of a WS_2/CoS_2 Heterostructure Electrocatalyst for Efficient Hydrogen Evolution at All pH Values. *ACS Sustainable Chem. Eng.* **2020**, *8* (11), 4474−4480.
(50) Mukherjee, P.; Sathiyan, K.; Vishwanath, R. S.; Zidki, T. Anchoring MoS_2 on an ethanol-etched Prussian blue analog for enhanced electrocatalytic efficiency for the oxygen evolution reaction. *Mater. Chem. Front.* **2022**, *6* (13), 1770−1778.
(51) Pan, L.; Jiao, C.; Liang, Y.; Xiong, J.; Wang, S.; Zhu, H.; Chen, G.; Song, H. In situ construction of MoS_2@CoS_2 spherical hydrangea-shaped clusters for enhanced visible-light photocatalytic degradation of sulfamethoxazole. *New J. Chem.* **2021**, *45* (12), 5645−5653.
(52) Chen, B.; Zhang, Q.; Zhao, P.; Cen, M.; Song, Y.; Zhao, W.; Peng, W.; Li, Y.; Zhang, F.; Fan, X. Coupled Co-Doped MoS_2 and CoS_2 as the Dual-Active Site Catalyst for Chemoselective Hydrogenation. *ACS Appl. Mater. Interfaces* **2023**, *15* (1), 1317−1325.
(53) Gao, S.; He, Y.; Li, H.; Yue, G.; Cui, Z.; Li, Y.; Bai, J.; Wang, N.; Zhang, Q.; Yu, Y.; et al. MoS_2@CoS_2 heterostructured tube-in-tube hollow nanofibers with enhanced reaction reversibility and kinetics for sodium-ion storage. *Energy Storage Mater.* **2024**, *65*, 103170.
(54) Yuan, J.; Huang, B.; Lu, Y.; Jiang, L.; He, G.; Chen, H. Ultrasensitive electrochemical detection of bisphenol A using composites of MoS2 nanoflowers, CoS_2 nano-polyhedrons, and reduced graphene oxide. *Environ. Chem. Lett.* **2022**, *20* (5), 2751−2756.
(55) Wang, X. *Study on Single-Atom Defect Design and Electrocatalytic Water Splitting Performance of Two-Dimensional MoS_2*. Dissertation, University of Science and Technology Beijing, 2023.
(56) Subbiah, V.; Landi, G.; Wu, J. J.; Anandan, S. MoS_2 coated CoS_2 nanocomposites as counter electrodes in Pt-free dye-sensitized solar cells. *Phys. Chem. Chem. Phys.* **2019**, *21* (45), 25474−25483.
(57) Huang, F.; Meng, R.; Sui, Y.; Wei, F.; Qi, J.; Meng, Q.; He, Y. One-step hydrothermal synthesis of a CoS_2@MoS_2 nanocomposite for high-performance supercapacitors. *J. Alloys Compd.* **2018**, *742*, 844−851.
(58) Deng, J.; Li, H.; Wang, S.; Ding, D.; Chen, M.; Liu, C.; Tian, Z.; Novoselov, K. S.; Ma, C.; Deng, D.; et al. Multiscale structural and electronic control of molybdenum disulfide foam for highly efficient hydrogen production. *Nat. Commun.* **2017**, *8* (1), 14430.
(59) Chen, Z.; Cummins, D.; Reinecke, B. N.; Clark, E.; Sunkara, M. K.; Jaramillo, T. F. Core−shell MoO3−MoS2 Nanowires for Hydrogen Evolution: A Functional Design for Electrocatalytic Materials. *Nano Lett.* **2011**, *11* (10), 4168−4175.
(60) Lee, S.; Benck, J.; Tsai, C.; Park, J.; Koh, A.; Abild-Pedersen, F.; Jaramillo, T.; Sinclair, R. Chemical and Phase Evolution of Amorphous Molybdenum Sulfide Catalysts for Electrochemical Hydrogen Production. *ACS Nano* **2016**, *10* (1), 624−632.
(61) Li, J.; Chen, L.; Liu, X.; Wen, Z.; Singh, C.; Yang, C.; Jiang, Q. Eggshell-like MoS2 Nanostructures with Negative Curvature and Stepped Faces for Efficient Hydrogen Evolution Reactions. *ACS Appl. Nano Mater.* **2021**, *4* (12), 14086−14093.

https://doi.org/10.1021/acsomega.4c10747
ACS Omega 2025, 10, 15129−15142